Turbulence measurements in nonpenetrative thermal convection

Ajay K. Prasad and P. V. Gonuguntla
Department of Mechanical Engineering, University of Delaware, Newark, Delaware 19716

(Received 8 March 1996; accepted 24 May 1996)

Nonpenetrative thermal convection at $\mathrm{Ra}=2\times10^7$ in a water layer of large-aspect ratio has been studied using Particle Image Velocimetry (PIV) to measure two-dimensional velocity vectors in a vertical plane. A sequence of 117 PIV photographs has been obtained with sufficient time separation between photographs to ensure statistical independence at least for the turbulent motions with time scales on the order of z_*/w_*. The grid spacing of the resulting velocity fields is adequate to resolve the smallest structures in the flow. Results include the development of motion with the onset of heating. The data set, obtained for fully developed turbulent flow, has been analyzed to obtain mean and rms velocities, vertical velocity skewness, two-point correlations, and stochastic estimates of velocity fields conditioned upon one and two-point events. A significant result is the absence of a discernible large scale circulation or mean flow with length scale on the order of the horizontal dimension of the fluid layer. Instead, the two-point correlations and stochastic estimates reveal the presence of roll cells whose horizontal length scale is equal to the layer depth. The measured values of vertical velocity skewness are in agreement with atmospheric measurements and large eddy simulations. The overall physical interpretation of the data suggests a seemingly chaotic and disordered motion, underlying which is a roll-cell mode with unit aspect ratio, punctuated by plumes emanating from the lower boundary. © *1996 American Institute of Physics.* [S1070-6631(96)02409-9]

I. INTRODUCTION

The atmospheric boundary layer plays host to extremely complicated flows, spanning a hugely diverse range of scales—from large-scale global circulation, to eddies on the order of millimeters. The atmosphere interacts with the ocean and the terrestrial surface leading to the transport of mass, momentum, and energy across the atmospheric boundary layer. The nature of these motions has long been the subject of meteorological research. However, since the atmospheric boundary layer depth is on the order of 1 km,[1] direct measurements are expensive and are subject to the vagaries of nature. While measurements have been accomplished by aircraft and balloon, laboratory models continue to provide a controlled environment for atmospheric research.

The standard laboratory model used by meteorologists consists of a shallow layer of fluid, heated from below and capped from above by a stably stratified layer.[2,3] The stable layer represents the inversion that caps the turbulent motions in the atmosphere. Over the course of the experiment, the heating at the lower boundary drives the turbulent motions in the form of plumes and thermals, which rise through the depth of the mixed or convecting layer and impact the base of the stable layer, and gradually erode it away. This model mimics the gradual erosion of the inversion layer in the atmosphere over the course of the day, due to the action of thermally induced motions arising from solar heating at the earth's surface.

The form of convection described above is called *penetrative* convection alluding to the penetration of the turbulent structures from the mixed layer into the stable inversion layer (see Fig. 1). Penetrative convection is inherently nonsteady owing to the increase of the convection layer depth over time. Direct numerical simulations and large eddy simulations of penetrative convection in the planetary boundary layer have been obtained by Moeng and Rotunno[4] and Moeng and Wyngaard,[5] respectively.

A second, familiar class of convection, called *Rayleigh–Bénard* convection occurs in a horizontal layer of fluid which is heated from below and cooled from above. As shown in Fig. 1 the two boundaries are maintained at fixed (but different) temperatures, and the average fluid temperature remains constant in time.

The literature contains numerous studies of Rayleigh–Bénard convection covering Rayleigh numbers from the critical value ($\mathrm{Ra}_c\approx2000$) when the flow just goes unstable, to $\mathrm{Ra}\approx10^{14}$ (Castaing *et al.*[6]). As described by Krishnamurti and Howard,[7] cellular convection with horizontal length scale comparable to the layer depth occurs for Ra just above Ra_c. At higher Ra, they observed that the cellular flow was replaced by a random array of transient plumes. Upon further increase, the plumes began to drift, resulting in a ''mean flow'' with the flow moving in one direction near the bottom and in the opposite direction near the top of the fluid layer. In this flow regime, the horizontal scale of motion is comparable to the layer width, as opposed to the layer depth at lower Ra. Krishnamurti and Howard[7] observed such mean flows at $\mathrm{Ra}\approx10^7$ at which point the flow is highly turbulent.

Numerical simulations of Rayleigh–Bénard convection are reasonably successful only at the lower Rayleigh numbers[8,9] (10 to 100 times Ra_c). As the Rayleigh number is increased, the simulations become considerably more difficult, and are open to questions about the chosen boundary conditions and aspect ratio dependence. For example, Balachandar *et al.*[10] used a computational box with a low aspect ratio of about 3, and with impermeable, stress-free boundary conditions at the upper and lower boundaries to simulate thermal convection at $\mathrm{Ra}=6.5\times10^6$. While Kerr[11] has con-

 1070-6631/96/8(9)/2460/11/$10.00

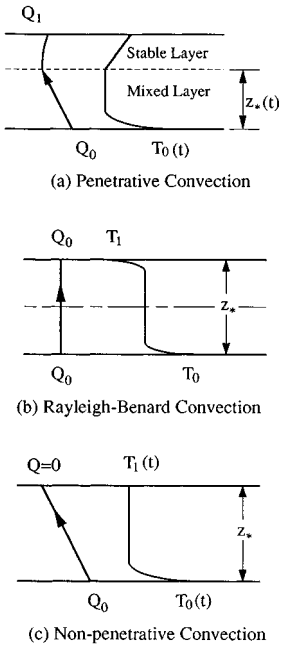

FIG. 1. Three classes of thermal convection [adapted from Adrian *et al.* (Ref. 12)].

ducted simulations up to $Ra=2\times10^7$ using more realistic no-slip boundary conditions at the upper and lower boundaries, high Ra simulation continues to pose a stiff challenge.

A third class of thermal convection, called *nonpenetrative* convection, occurs when a constant heat flux is applied at the lower boundary and the upper boundary is insulated. As shown in Fig. 1 the boundary conditions in nonpenetrative convection share common features with those of penetrative convection as well as Rayleigh–Bénard convection.

On the one hand, the insulating upper boundary in nonpenetrative convection may be considered as an idealization of the capping inversion layer of penetrative convection. On the other, nonpenetrative convection may provide an easier platform to study thermally induced turbulence convection, simply because plume formation occurs only at the lower boundary. In contrast, Rayleigh–Bénard convection experiences plume formation at both boundaries leading to a flow field that is more complicated to measure and interpret.

Unlike penetrative and Rayleigh–Bénard convection, nonpenetrative convection has not received much attention from researchers, with the exception of a few experimental[12,13] and numerical[4] studies.

Significance of nonpenetrative convection. Nonpenetrative convection, by the nature of its boundary conditions, shares common features with penetrative convection, as well as Rayleigh–Bénard convection. For example, both nonpenetrative and penetrative forms are nonsteady with the fluid temperature increasing in time, and with similar temperature conditions at the lower boundary, and (to first order) the upper boundary as well. Both forms have a convecting layer which is capped from above, such that regions of upward-moving fluid collide with the capping layer resulting in the transformation of vertical to horizontal kinetic energy.

The agreement of the statistical moments in penetrative and nonpenetrative forms of convection has been explained by Sorbjan.[14] He states that any statistical moment involving the velocity, temperature, or concentration of a passive species may be decomposed into two components, the nonpenetrative and the residual

$$X=X_b+X_t,$$

where b refers to the nonpenetrative component and t to the residual component (penetrative minus nonpenetrative). It transpires that the statistical moments in penetrative and nonpenetrative convection are very similar, except in the upper part of the convective boundary layer. Sorbjan[14] asserts that the deviation of the penetrative values near the upper part of the convective layer from the corresponding nonpenetrative values are due to the effects of entrainment of the stable layer in the former, whereas the agreement is very good over the rest of the convective layer.

Nonpenetrative convection also shares similarities with Rayleigh–Bénard convection owing to the fact that the upper boundary is a solid wall, as opposed to the mobile (albeit stably stratified) capping fluid layer in penetrative convection. It is sometimes useful to consider nonpenetrative convection as one-half of the Rayleigh–Bénard problem, i.e., the region between the lower boundary and the midplane in Rayleigh–Bénard convection exhibits similarities at least insofar as the mean temperature profile is concerned. Yet, plume formation in nonpenetrative convection occurs only at the lower boundary (as opposed to both boundaries in Rayleigh–Bénard) convection, and hence the flow should be easier to interpret.

Siggia[15] presents a review of the current level of knowledge of high Rayleigh number convection owing to recent experiments and numerical simulations. He concludes that *experiments remain the pre-eminent mode of enquiry* at high Ra's. Our experimental study has applied the modern diagnostic technique of PIV which yields accurate, instantaneous velocity data over extended domains. The current data set provides a detailed physical picture of the flow based on over a hundred instantaneous 2-D realizations in a vertical plane. In addition, statistical results include mean and rms velocity profiles, vertical velocity skewness as a function of depth, two-point spatial correlations for velocity, and stochastic estimates of the flow field.

One of our goals in this study was to investigate the existence of large-scale mean flow in thermal convection of a large aspect ratio fluid layer. By mean flow we imply large-scale motions whose length scale is on the order of the *horizontal* dimension of the fluid layer. Experimental observations of such mean flows have been listed for Rayleigh–Bénard convection by Krishnamurti and Howard[7] for $Ra>10^6$ in the case of water, and for $Ra>10^7$ for high Prandtl number fluid. Siggia[15] reviews 12 thermal convection experiments; of these, 6 report mean flows, which is indicative of the uncertainty surrounding this phenomenon. The review reveals that mean flows occur more readily in small aspect ratio fluid layers. For example, Castaing *et al.*[6] (for $Ra>10^8$), Wu and Libchaber[16] (for $Ra>10^7$), and Zocchi *et al.*[17] (for $Ra\approx10^9$) all report the presence of mean flows in fluid layers of aspect ratio of order unity. While recircula-

tions on the order of the fluid layer *depth* can be referred to as mean flow in a small-aspect ratio container, in this study, we focus on the large-aspect ratio situation. Numerical simulations of high Ra convection have been performed by Balachandar *et al.*[10] (Ra=6×10^6, aspect ratio ~3), and Kerr[11] (Ra=2×10^7, aspect ratio ~6). The latter is perhaps the most realistic simulation to date owing to the use of no-slip boundary conditions at the top and bottom boundaries as opposed to the free-slip or stress-free boundary conditions used by Balachandar *et al.*[10] However, while Balachandar *et al.*[10] observes the presence of a large-scale circulation containing 25% of the total energy and with a lifetime of about 40 large eddy turnover times, Kerr[11] reports that ''large-scale shears'' are not observed.

The occurrence of such mean flows has been the subject of some debate amongst experimentalists: For instance, is the mean flow a manifestation of symmetry breaking (albeit in a flow that is already highly turbulent) or is it an artifice produced by poorly enforced boundary conditions? How much of a perturbation is adequate to trigger such mean flows? What role does the aspect ratio have in this regard? Krishnamurti and Howard[7] took extreme care to eliminate possible sources for bias in their boundary conditions and still observed a mean flow which persisted in spite of attempts to alter their direction, such as tilting the test section, drawing paddles mechanically through the flow, etc.

In spite of the recent focus on mean flows[15] work remains to be done in understanding the mechanisms by which mean flows are generated and sustained, their interaction with thermals, and the transport of heat from the lower boundary.

II. EXPERIMENTAL APPROACH

This section describes the experimental test section, and the PIV technique which provided the velocity measurements.

A. Description of test section

A large-aspect ratio test section (60 cm×60 cm×15 cm high) was constructed for the investigation of nonpenetrative convection. The height of the working fluid is variable; our baseline height was 7.62 cm, giving a width-to-height aspect ratio of order 10. At this large aspect ratio, end effects should be minimized, allowing a more reliable extrapolation to the infinite domain. The lower plate is a 7.5 cm thick aluminum plate with 48 equispaced, 2.5 mm deep grooves cut into its lower surface. An electrical heating element consisting of 30 m of 28 AWG Teflon insulated hook-up wire was press fitted into the grooves. Good thermal contact between the wire and the aluminum block was ensured by coating the wire with high temperature grease. Finally, a length of O-ring material was press fitted into each groove to prevent the leakage of the grease over time. A schematic of the test section is shown in Fig. 2.

Care was taken during the design and fabrication phase to enforce uniformity of boundary conditions (geometry and heat flux). For instance, a thick aluminum plate was chosen for the lower boundary to allow possible nonuniformities of input heat flux to damp out via horizontal diffusion. Second,

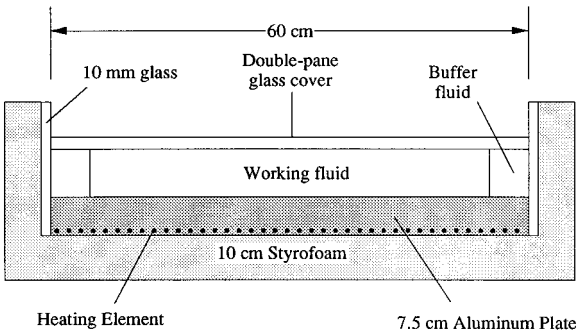

FIG. 2. Schematic of nonpenetrative convection test section.

in order to better enforce the insulating conditions at the side walls, we have incorporated an auxiliary heater along the edge of the aluminum plate to compensate for the sensible heat gain of the glass side walls during the experiment. The correct value for the auxiliary heating was determined by numerical simulation. Finally, since it is impossible to completely eliminate sensible heating of the side walls (which precludes a truly insulating condition) we have created a ''box-inside-a-box'' design as shown in Fig. 2. Then, the experiment is conducted within the confines of the *inner* box measuring 50 cm×50 cm (aspect ratio=6.6), and the (convecting) fluid in the annular region between the inner box and the side walls acts as a *buffer* region with superior insulation characteristics. It should be noted that fluid motions adjacent to the lower boundary can cause local fluctuations in the heat transfer coefficient, resulting in local fluctuations in temperature and/or heat flux at the lower boundary. The high thermal conductivity of the aluminum plate should help to damp out these these fluctuations, however, we have not attempted to quantify the magnitude of these fluctuations.

The side walls of the test section were constructed from 10 mm thick plate glass to allow optical access to the flow. Similarly the upper boundary comprises of a double pane plate glass window, which provides optical access for plan form observations, while enforcing the insulating boundary condition. Owing to the sensible heat gain of the glass cover, a truly insulating condition at the upper boundary is not realized. However, calculations show that this effect is small. The heat flux for the experiments reported here was set at approximately 600 W/m^2. Only a portion of this heat flux reaches the fluid, rest being used to heat the aluminum plate, side walls, etc. Consequently, the rate of temperature rise of the water was 0.156 °C/min, resulting in a kinematic heat flux of 0.198 °C mm/s. The convective velocity w_* given by

$$w_* = (g\alpha Q_0 z_*)^{1/3}$$

was 3.3 mm/s. Here, g is the acceleration due to gravity, α is the thermal coefficient of expansion, Q_0 is the kinematic heat flux, and z_* is the height of the fluid layer. The Rayleigh number given by $g\alpha(T_b - T_m)z_*^3/\nu\kappa$ was 2×10^7, where T_b and T_m are the temperatures of the lower boundary and the mixed layer respectively, ν is the kinematic viscosity, and κ is the thermal diffusivity.

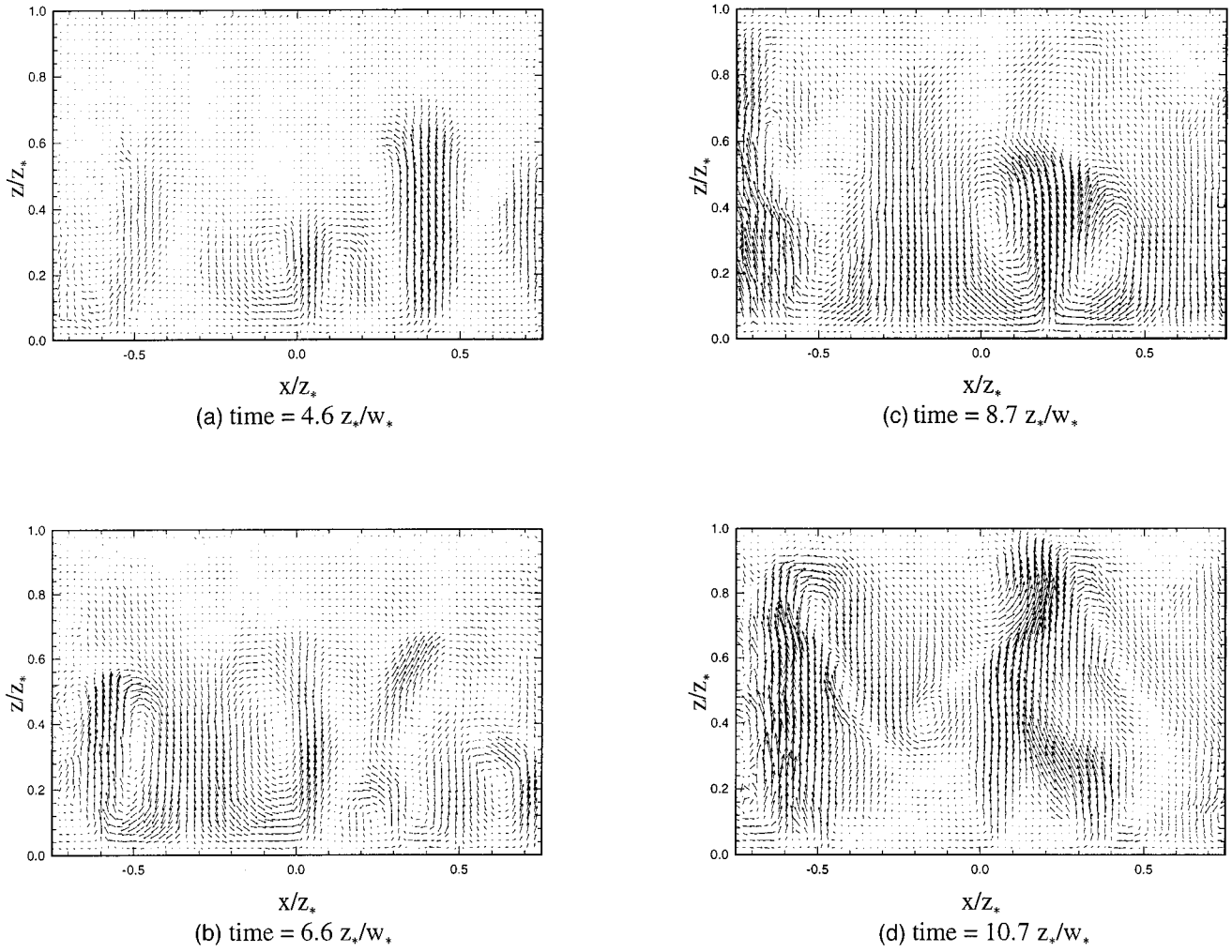

FIG. 3. Sequence of frames indicating the onset of thermal convection; times are normalized with the convective time scale, $z_*/w_*=23s$.

B. Particle image velocimetry

PIV consists of seeding a flow with small tracer particles, and illuminating a planar slice of the flow with two pulses of laser light. The laser light is scattered by the tracer particles and the images are captured through a lens on to photographic film or a charge coupled device (CCD) camera. Since there are two images per particle, corresponding to each pulse of laser light, the local velocity of the fluid is obtained by determining the displacement of the two images in a given pair, and dividing that displacement vector by the time separation between laser pulses, as described by Adrian.[18]

Since we use high seeding densities of the tracer particles for increased resolution, it becomes difficult to directly match the two images corresponding to a given pair. Therefore, a statistical approach is required. In this approach, a small (typically 1 mm×1 mm) region of the photograph (called an ''interrogation spot'') containing 10 to 20 pairs of images is digitized and cross correlated with a second spot which is displaced from the first one by an amount equal to the local displacement vector. The spatial cross correlation, $C(\mathbf{S})$, between the intensity distribution of the first spot, $I_1(\mathbf{X})$, and the second spot, $I_2(\mathbf{X})$, is given by

$$C(\mathbf{S})=\int_{\text{spot}} I_1(\mathbf{X})I_2(\mathbf{X}+\mathbf{S})d\mathbf{X}.$$

The location of the signal peak in the cross-correlation plane is proportional to the magnitude and the direction of the velocity vector corresponding that interrogation spot. Thus the technique averages the data over the given spot and this makes it especially robust. A typical photograph can yield on the order of thousands of vectors. Since the direct computation of the cross-correlation function is compute intensive, an FFT-based technique is used.

Our PIV system consists of Alacron FT200 boards utilizing two Intel i860 processors integrated into a 486-DX2, 66 MHz computer giving 200 Mflops of image processing speed. The system performs a 128×128 real to complex FFT in under 6 ms, and can interrogate PIV images at the rate of 50 vectors per second.

For the experiments described here, the illumination was provided by a mechanically chopped Ar-ion laser whose beam was formed into a 1 mm thick sheet. The separation between pulses was 62 ms and the images were acquired at a

magnification of 0.24, by a Nikon F3 camera and a Micro-Nikkor 55 mm lens, using an f stop of 8 and TMAX 400 film. The scattering particles consisted of 8 μm glass microbubbles, which could be retained in suspension for long periods. Directional ambiguity was removed by translating the camera horizontally between exposures[19] at a velocity equal to $2.6w_*$. The digitized images were analyzed using the cross-correlation algorithm and the resulting vector fields contained vectors on a Cartesian grid with a grid spacing of 2.5 mm in the flow.

The uncertainty in the velocity measurement is 1% to 2% of w_*. The use of image shifting extends the range of measurable velocities to $-2.0w_*<u$, $w<2.0w_*$. u and w are the velocities in the horizontal and vertical directions, respectively. The dynamic range, defined by the ratio of the largest measurable velocity to the smallest, is determined by the accuracy of the technique. In this experiment the dynamic range was on the order of 100.

III. RESULTS

Figure 3 is a sequence of vector maps showing the onset of thermal convection with the commencement of heating. It takes about 100 s for the heat flux to diffuse through the aluminum block, and for the conduction layer in the fluid to grow to a point where the thermal instability sets in and fluid motion commences. The vector maps shown in Fig. 3 follow the evolution of the plumes as they grow and rapidly become turbulent. The resolution of the vector maps in Fig. 3 is higher (70×47) than the following data. The lower and upper edges of the vector plots coincide with the lower and upper boundaries of the fluid layer.

A. Mean and rms profiles

Statistical quantities were extracted from photographs which were recorded 10 min after the onset of convection corresponding to about 26 convective time scales (z_*/w_*), by which time the turbulent flow is fully established. Each run consisted of about 30 realizations, with a spacing of 1 min (2.6 convective time scales) between realizations. The experiment was halted at the end of 30 realizations, by which time the test section warmed up by about 6 °C. A total of four such runs were conducted, generating a total of 117 realizations. Each realization produced a horizontal by vertical grid of 48×32 vectors, in a vertical plane located at the center of the test section, and spanning the depth of the fluid layer.

Ensemble averaged u (horizontal) and w (vertical) velocity profiles were obtained by averaging along the rows of all realizations recorded during each run. Figures 4(a) and 4(b) show that the mean u and w velocities are quite small, and that the variations from run to run are small enough (about $0.15w_*$) to indicate that gross differences were absent. Figures 4(a) and 4(b) also show the ensemble averaged rms velocity profiles, σ_u and σ_w, for each run. Again, the day to day variations are small (about $0.1w_*$ for σ_u and $0.05w_*$ for σ_w), showing that the convecting fluid retains its ergodicity from run to run. It is expected that the incorporation of additional realizations into the mean and rms profile for each day would drive down the day-to-day variations further; i.e., the day-to-day variations most likely result from inadequate sampling. However, the variations decrease as $\sqrt{N}$ where N is the number of realizations, and we were limited to about 30 realizations per day owing to possible overheating of the test section.

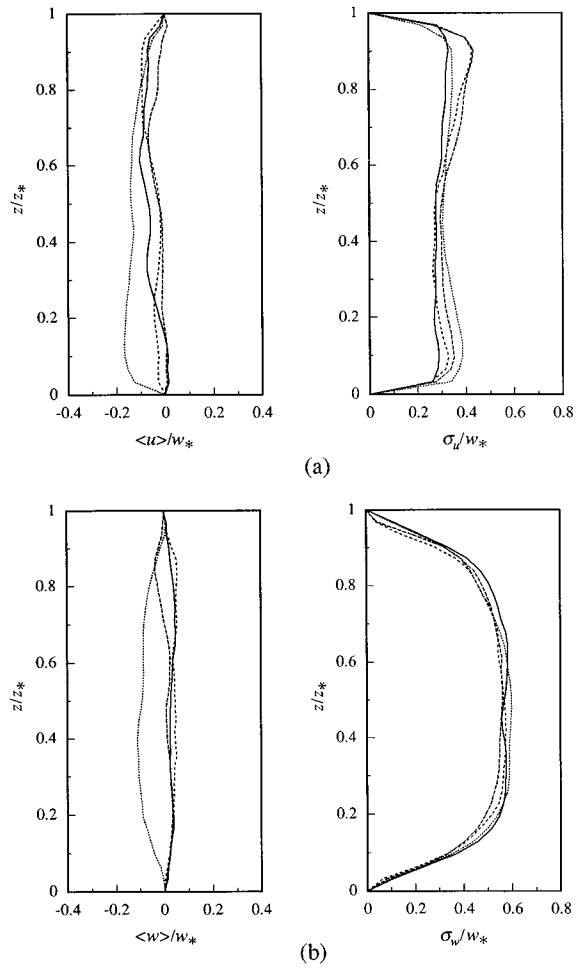

FIG. 4. Mean and rms profiles for (a) u and (b) w for each of the four runs.

Figure 5 shows the mean and rms velocity profiles for u and w averaged over all 117 realizations. Averaging over all four days has driven $\langle u\rangle$ down to about 5% to 10% of w_*: In accordance with sampling theory, increasing the sample size by four has helped $\langle u\rangle$ to converge to the ideal value of 0 by roughly a factor of 2. The mean value for w is negligible. It should be noted that w_* is a characteristic velocity scale; local velocities can and do exceed w_*.

It therefore appears that the design of the test section and the experimental conditions of our experiment are such that significant mean flows are not established at least for the chosen Rayleigh number of 2×10^7. This was confirmed by several hours of flow visualization, not only in the plane in which PIV measurements were obtained, but over several other planes inside the fluid layer. Our results are in contrast to those of Krishnamurti and Howard[7] who observed persistent mean flows in a large-aspect ratio container of water at $\mathrm{Ra}=2.4\times10^6$. They observed that the mean flow consisted of a flow moving in one direction near the bottom and in the opposite direction near the upper boundary, and was strong

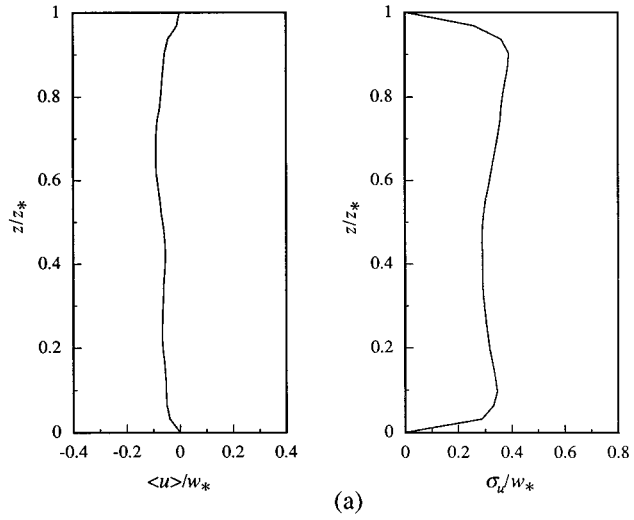

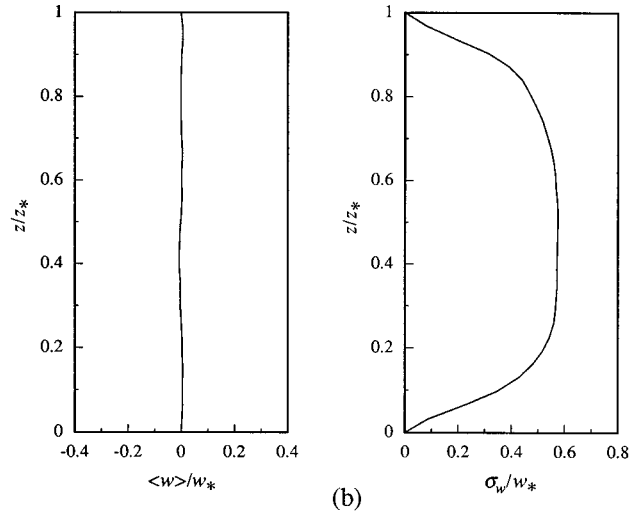

FIG. 5. Mean and rms profiles for (a) u and (b) w for all of the four runs.

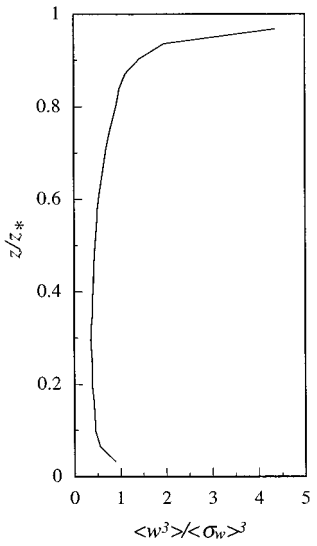

FIG. 6. Vertical velocity skewness averaged over all four runs.

enough to overcome attempts to alter their direction, such as tilting the test section, or drawing paddles through the flow. They fitted this ''S-shaped'' mean flow profile with a sine function with the origin located at $z=z_*/2$, and an amplitude of 1 mm/s, which we estimate to be about 60% of w_*. The mean flow in our experiment does not show this characteristic ''S'' profile, and further, our maximum value is about 1 order of magnitude smaller. At present, we do not have a conclusive explanation for the lack of a mean flow in our experiment, other than the physical differences in the manner in which the boundary conditions were designed. The lack of such a mean flow in our experiment has allowed us to plan a series of experiments to deliberately destabilize the fluid layer, either mechanically or thermally, in order to correlate the size of the perturbation with the strength and persistence of the resulting mean flow. With the help of PIV measurements, we intend to probe the mechanisms which cause the generation and sustenance of mean flows. These results will be reported in the future.

The profiles of σ_u and σ_w are in good agreement with those obtained by Adrian *et al.*[12] from experiments in nonpenetrative convection. There is also good agreement with Kerr's[11] simulations of Rayleigh–Bénard convection at Ra$=2\times10^7$. The σ_u profile displays two characteristic maxima adjacent to the boundaries. Near the lower boundary, the maximum arises because fluid is drawn horizontally into the base of the plume from all directions, resulting in a local increase in horizontal kinetic energy. Near the upper boundary, the maximum is due to the impact of the rising plume with the upper boundary, resulting in a conversion of kinetic energy from the vertical to the horizontal direction. Conversely, the σ_w profile indicates that the vertical kinetic energy is small at the lower boundary, increases as the plume rises through the mixed layer, and then decreases as it approaches the upper boundary.

B. Vertical velocity skewness

Figure 6 shows the vertical velocity skewness (S_w) obtained by ensemble averaging all 117 realizations. It is apparent that $S_w(z)$ is positive for all z. This is to be expected for nonpenetrative convection, where the flow (for all z) consists of less-frequent narrow, intense plumes representing large positive w excursions, surrounded by more frequent, lower speed, cooler descending fluid. In contrast, $S_w(z)$ in Rayleigh–Bénard convection should show an antisymmetric behavior about the central ($z=0.5z_*$) plane owing to antisymmetric top and bottom temperature boundary conditions. The Rayleigh–Bénard simulation of Balachandar[10] does agree with Kerr's[11] as far as the antisymmetric nature is concerned. Otherwise, however, these two simulations differ significantly from each other. For example, Balachandar's results for Ra$=6.5\times10^6$ indicate that $S_w(z)$ experiences a positive peak ($=0.14$) at $z/z_*=0.14$, and decreases almost linearly through the height of the mixed layer with a second peak of height -0.16 at $z/z_*=0.9$, i.e., the slope of the skewness profile is about -0.4 through the mixed layer. In contrast Kerr's[11] results show that the slope of $S_w(z)$ in the mixed layer is *positive* for Ra$=5\times10^4$ and 10^6, although the slope decreases with increasing Ra. For Ra$=2\times10^7$ S_w is practically zero through the entire mixed layer region, and is expected to remain zero[11] for higher Ra. The differing trends

between the $S_w(z)$ profiles of Kerr and Balachandar have been attributed[11] to the fact that Kerr used no-slip velocity boundary conditions at the top and bottom boundaries, whereas Balachandar applied free slip.

Moeng and Rotunno[5] examined the issue of vertical velocity skewness in greater detail by performing a $(96)^3$ large-eddy simulation of the planetary boundary layer. They discovered that $S_w(z)>0$ for all z, increasing slowly with z through the mixed layer, and then increasing more rapidly adjacent to the inversion layer. Their results are in reasonable agreement with atmospheric data, where $S_w>0$ for all z, but with a more or less constant value of about 0.6 through the mixed layer.[4,5] Our experiments, which are an idealization of the planetary boundary layer in that the inversion layer has been replaced by a rigid boundary, show a good match with the results of Moeng and Rotunno,[4] as well as the atmospheric measurements.[5]

One of the puzzling features of S_w observed in Rayleigh–Bénard convection is that, S_w is negative very close to the lower boundary, and positive very close to the upper boundary.[10,11] An apparent paradox arises due to the following argument: Adjacent to the lower boundary, the dominant flow structure is the thermal plume, which consists of hot, intense, and less-frequent upward-moving fluid, which should lead to *positive* S_w there. Similarly, adjacent to the upper boundary we should see cold, intense, descending plumes, contributing to a *negative* S_w. Why, then, do simulations and measurements show the opposite trend?

The answer may be found in our $S_w(z)$ profiles. In our bottom-heated, nonpenetrative case, we see that S_w is indeed positive adjacent to the lower boundary. As z increases, S_w decreases somewhat, but is still positive. Adjacent to the upper boundary, S_w increases very rapidly, and assumes values that are substantially larger than those seen near the lower boundary. This is a clear indication that although plumes form along the lower boundary, they continue to maintain their integrity as they move up through the mixed layer and even as they approach close to the upper boundary. In fact, these upward moving plumes actually cause larger S_w at the upper boundary as compared to the lower boundary.

The nonpenetrative configuration described in the preceding paragraph has been referred to as ''bottom-up'' diffusion[20] implying introduction of a species through an area source at the bottom with zero flux at the top. In contrast, the ''top-down'' diffusion case consisting of a cooled upper boundary and an insulated lower boundary should exhibit S_w which is always negative and becomes more so with decreasing z.[4] If, as suggested by Moeng and Rotunno,[4] the two situations are superimposed to retrieve Rayleigh–Bénard convection, then the resulting skewness profile should show negative skewness close to the lower boundary, zero skewness in the mixed layer and positive skewness near the upper boundary, consistent with the results of Kerr.[11] On a cautionary note, it should be remembered that the superposition of top-down and bottom-up diffusion does not automatically reproduce Rayleigh–Bénard convection because the interaction of rising and falling plumes in the latter can be important.

C. Two-point velocity correlations

Two-point correlations were computed using the total database of 117 realizations according to

$$R_{u_1u_2}(x,z_1,z)=\frac{1}{NI}\sum_{1}^{N}\sum_{i=1}^{I}u_1(x',z_1)u_2(x'+x,z), \quad (1)$$

where x is the horizontal separation between the first point located at z_1 and the second point located at z. $x'=(i-1)\Delta x'$, where $\Delta x'$ is the horizontal grid spacing of the 2-D vector field; the maximum value of x', i.e., the horizontal length of the vector field, is X'. In Eq. (1), $I=(X'-|x|)/\Delta x'+1$, is the number of data points contributing to each average. The range of the separation x was restricted to $\pm X'/2$ in order to retain adequate data in the average. N is the total number of realizations $(=117)$.

The velocities u_1 and u_2 in Eq. (1) are total, instantaneous values; the ensemble mean velocity has *not* been subtracted. Furthermore, symmetries—such as $R_{uu}(x,z)=R_{uu}(-x,z)$; $R_{uw}(x,z)=-R_{uw}(-x,z)$; $R_{wu}(x,z)=-R_{wu}(-x,z)$; and $R_{ww}(x,z)=R_{ww}(-x,z)$—were not forced during the calculation of the two-point correlations. All velocities were normalized by w_*.

Figures 7(a), 7(b), and 7(c) show the R_{uu} correlation between the u velocity at $z/z_*=2/31$, 16/31, and 29/31, respectively, and the u velocity over the rest of the field. Figure 7(a) shows that the correlation is positive for $z<0.5z_*$ and negative for $z>0.5z_*$, implying that the horizontal flow is, on average, in opposite directions across the central plane of the fluid layer implying the existence of a roll cell. However, the correlation decreases rapidly in the x direction, and changes sign at $x=\pm 0.5z_*$ suggesting that, buried beneath the turbulent and chaotic nature of the flow is a structure roughly resembling a unit-aspect ratio roll cell. Had a large-scale circulation on the order of the horizontal dimension of the fluid layer existed, the R_{uu} correlation would persist for very much larger values of x. This result corroborates the u and w mean profiles which also indicate that a large-scale circulation does not exist in our flow.

Figures 8(a), 8(b), and 8(c) show the R_{ww} correlation between the w velocity at $z/z_*=2/31$, 16/31, and 29/31, respectively, and the w velocity over the rest of the field. The correlation is elongated in the vertical direction, suggesting that the thermal plume is a dominant structure. Furthermore, the correlation persists all the way from one boundary to the other, supporting the argument for the large positive S_w at the upper boundary. The R_{ww} correlation field for $z/z_*=16/31$ is highly symmetric, indicating that this statistic is well converged.

Figures 9(a), 9(b), and 9(c) show the R_{wu} correlation for the w velocity at $z/z_*=2/31$, 16/31, and 29/31, respectively, with the u velocity over the rest of the field. There exist two horizontally elongated lobes of positive and negative correlation to the left and right, respectively, for $z/z_*=2/31$. The interpretation is that the vertical velocity at that point is fed by strong incoming horizontal velocities. In other words, the fluid contained in an ascending plume is drawn inwards from all directions adjacent to the lower boundary. This explains the peak in the σ_u profile in the vicinity of the lower bound-

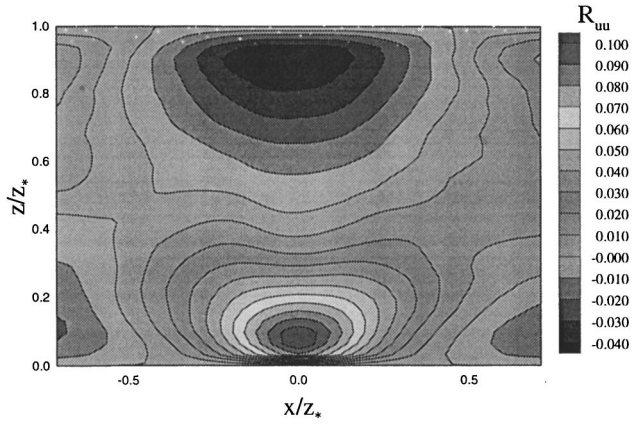

(a) $z/z_* = 2/31$

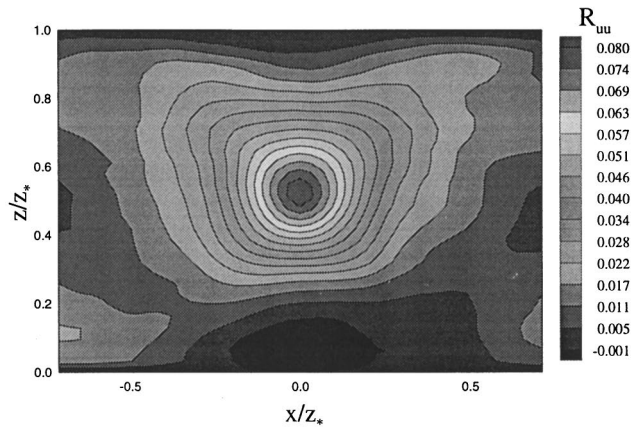

(b) $z/z_* = 16/31$

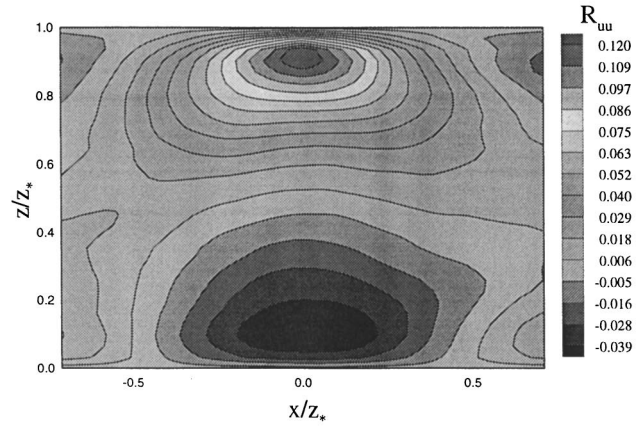

(c) $z/z_* = 29/31$

FIG. 7. R_{uu} correlations for (a) $z/z_*=2/31$; (b) $z/z_*=16/31$; (c) $z/z_*=29/31$.

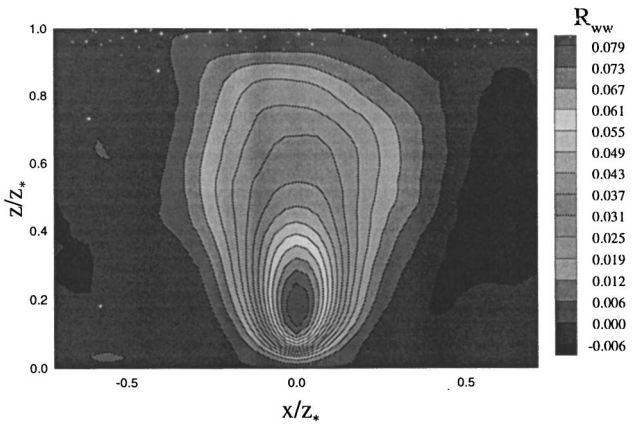

(a) $z/z_* = 2/31$

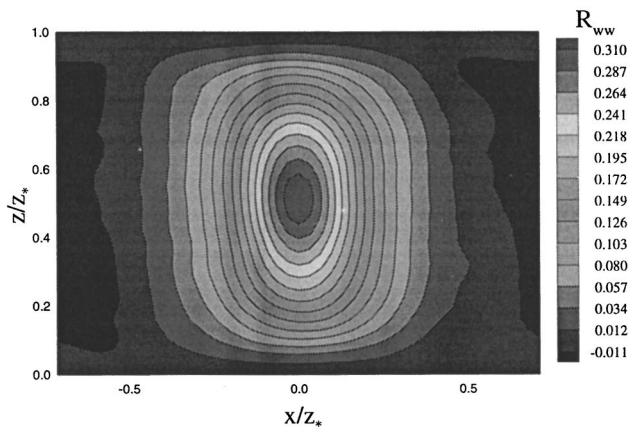

(b) $z/z_* = 16/31$

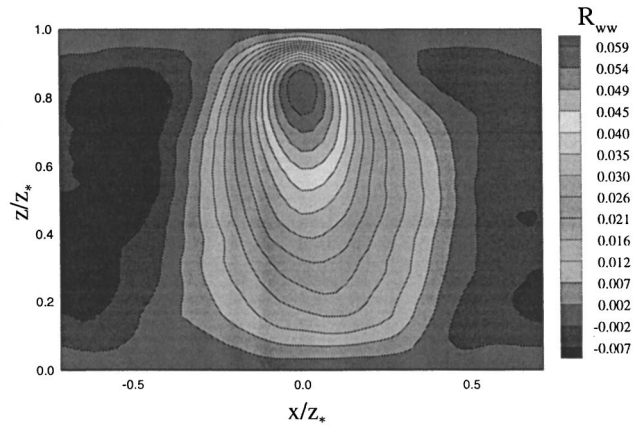

(c) $z/z_* = 29/31$

FIG. 8. R_{ww} correlations for (a) $z/z_*=2/31$; (b) $z/z_*=16/31$; (c) $z/z_*=29/31$.

ary. Similarly, in Fig. 9(c) the elongated lobes of positive and negative correlation lie to the right and left, respectively, of the chosen point indicating that when the plume impacts the upper boundary, it spreads outwards in all directions, resulting in a conversion of vertical kinetic energy to horizontal kinetic energy. Consequently, one finds a corresponding peak in the σ_u profile adjacent to the upper boundary. Figure 9(b) again indicates that a vertical velocity at the central plane is fed by horizontal velocities of the appropriate sign along the lower boundary and causes a horizontal spreading upon impact at the upper boundary.

The high degree of symmetry in the correlation fields indicates that the correlation statistics are adequately converged.

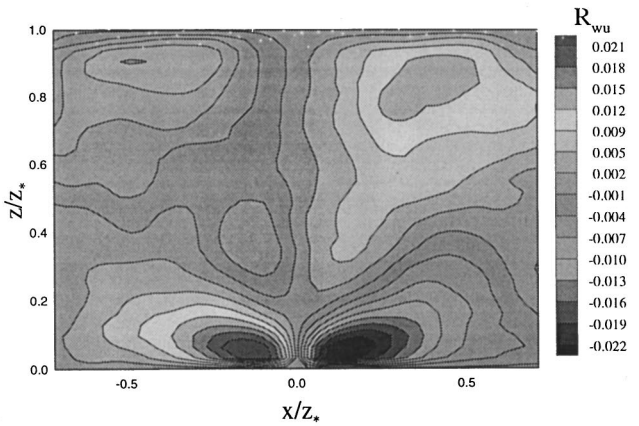

(a) $z/z_* = 2/31$

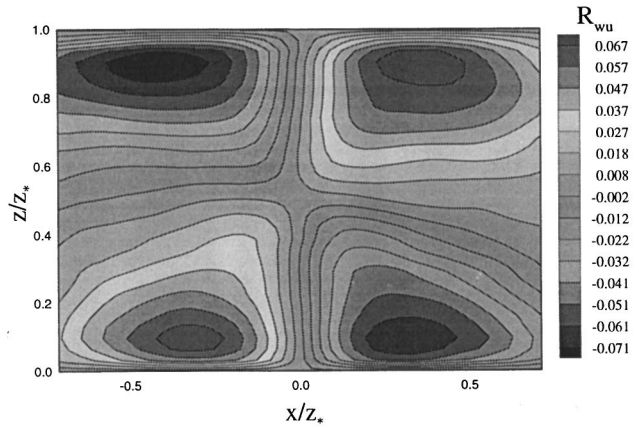

(b) $z/z_* = 16/31$

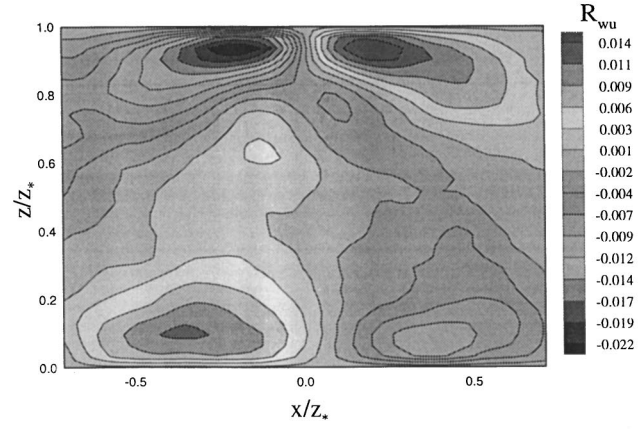

(c) $z/z_* = 29/31$

FIG. 9. R_{wu} correlations for (a) $z/z_*=2/31$; (b) $z/z_*=16/31$; (c) $z/z_*=29/31$.

D. Stochastic estimates

One of the techniques for educing the dominant flow structure in a turbulent flow is stochastic estimation.[21] Stochastic estimation is similar to conditional averaging in which an event vector is specified and a vector field surrounding the event vector is obtained by averaging *only* those realizations which contain the specified vector, i.e., the average is conditional upon the realizations containing the specified vector.

However, stochastic estimation differs from conditional averaging in that in the former, the vector field that is predicted around a specified event uses *all* of the available data, such that the difference between the predicted field and all of the data is minimized in a least-squares sense.

Let $u_i(\mathbf{x}')$ represent all of the available data. If the specified event vector is $u_j(\mathbf{x})$, and the vector field predicted by stochastic estimation is $\hat{u}_i(\mathbf{x}')$, then we may write:

$$\hat{u}_i(\mathbf{x}') = A_{ij}(\mathbf{x}',\mathbf{x})u_j(\mathbf{x}),$$

where $A_{ij}(\mathbf{x}',\mathbf{x})$ is the coefficient matrix. The error e_{ij} between the estimated field and the data is given by

$$e_{ij} = \langle [u_i(\mathbf{x}') - \hat{u}_i(\mathbf{x}')]^2 \rangle = \langle u_i(\mathbf{x}') - A_{ij}(\mathbf{x}',\mathbf{x})u_j(\mathbf{x}) \rangle^2.$$

The error is minimized by choosing A_{ij} such that $\partial e_{ij}/\partial A_{ij}=0$. The resulting condition is

$$\langle [u_i(\mathbf{x}') - A_{ij}(\mathbf{x}',\mathbf{x})u_j(\mathbf{x})]u_k(\mathbf{x}) \rangle = 0.$$

Thus the mean square error is minimized by choosing A_{ij} such that the error $(u_i' - A_{ij}u_j)$ is statistically orthogonal to u_k. A_{ij} is then determined by using the two-point correlations according to

$$A_{ij}(\mathbf{x}',\mathbf{x}) = \langle u_i(\mathbf{x}')u_k(\mathbf{x}) \rangle \langle u_j(\mathbf{x})u_k(\mathbf{x}) \rangle^{-1}.$$

Finally,

$$\hat{u}_i(\mathbf{x}') = \langle u_i(\mathbf{x}')u_k(\mathbf{x}) \rangle \langle u_j(\mathbf{x})u_k(\mathbf{x}) \rangle^{-1} u_j(\mathbf{x}).$$

The estimated field $\hat{u}_i(\mathbf{x}')$ is such that its mean square error with respect to the measured data has been minimized. It is the best mean square estimate.

If the specified event is a single point event, $\langle u_j u_k \rangle$ is a 2×2 matrix

$$\langle u_j u_k \rangle = \begin{bmatrix} \langle u_1 u_1 \rangle & \langle u_1 u_2 \rangle \\ \langle u_2 u_1 \rangle & \langle u_2 u_2 \rangle \end{bmatrix},$$

where $u_1 = u$ and $u_2 = w$. If a two-point event is specified, $\langle u_j u_k \rangle$ is a 4×4 matrix

$$\langle u_j u_k \rangle = \begin{bmatrix} \langle u_1^1 u_1^1 \rangle & \langle u_1^1 u_2^1 \rangle & \langle u_1^1 u_1^2 \rangle & \langle u_1^1 u_2^2 \rangle \\ \langle u_2^1 u_1^1 \rangle & \langle u_2^1 u_2^1 \rangle & \langle u_2^1 u_1^2 \rangle & \langle u_2^1 u_2^2 \rangle \\ \langle u_1^2 u_1^1 \rangle & \langle u_1^2 u_2^1 \rangle & \langle u_1^2 u_1^2 \rangle & \langle u_1^2 u_2^2 \rangle \\ \langle u_2^2 u_1^1 \rangle & \langle u_2^2 u_2^1 \rangle & \langle u_2^2 u_1^2 \rangle & \langle u_2^2 u_2^2 \rangle \end{bmatrix}.$$

For a two-point event, the superscripts 1 and 2 refer to the first and second points, respectively.

Figure 10 is a stochastic estimate based on a single point event vector is located at $(x/z_*=0,\ z/z_*=2/31)$ with $u=1$ and $w=0$. The estimated field indicates a roll cell, whose horizontal extent is roughly equal to the fluid layer depth z_*, and essentially reflects the R_{uw} correlation in Fig. 7(a).

Figure 11 is a stochastic estimate based on a single-point event located at $(x/z_*=0,\ z/z_*=2/31)$ with $u=0$ and $w=1$. The estimated field indicates a plume which extends all the way from the lower boundary to the upper boundary. The horizontal inward streaming of fluid into the base of the

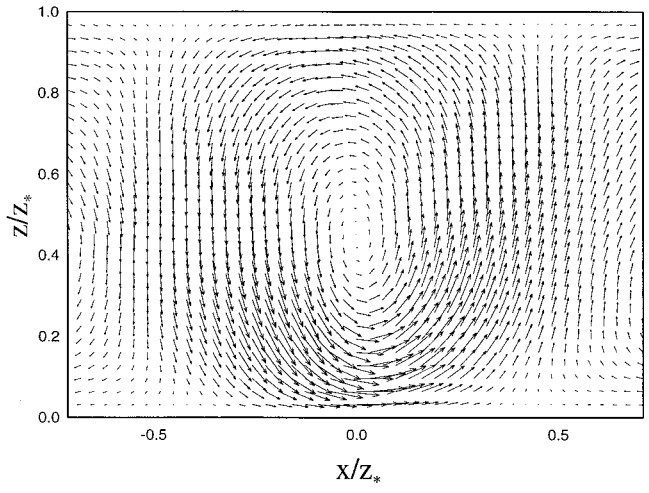

FIG. 10. Single point stochastic estimate with event vector (1,0) located at $(x/z_*=0,\ z/z_*=2/31)$.

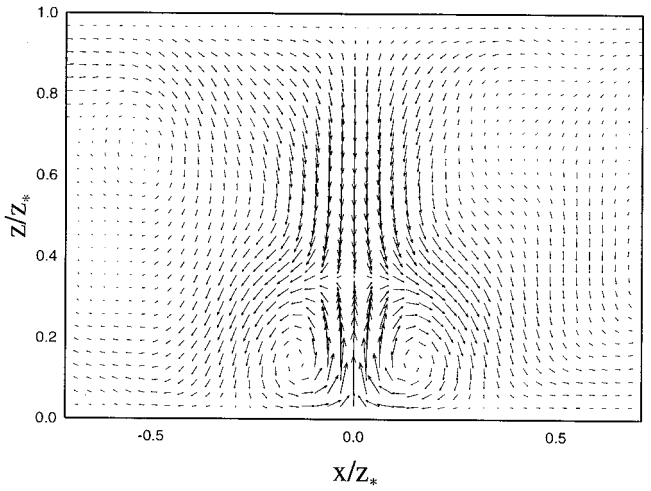

FIG. 12. Two point stochastic estimate with event vectors (0,1) located at $(x/z_*=0,\ z/z_*=2/31)$, and $(0,-1)$ located at $(x/z_*=0,\ z/z_*=16/31)$.

plume is clearly evident, as is the horizontal spreading upon impact with the upper boundary, reflecting the R_{ww} correlation of Fig. 8.

Figure 12 is a stochastic estimate based on a two-point event. The first point located at $(x/z_*=0,\ z/z_*=2/31)$ has $(u,w)=(0,1)$ and the second point located at $(x/z_*=0,\ z/z_*=16/31)$ has $(u,w)=(0,-1)$. The resulting structure clearly depicts a mushroom shaped plume forming at the lower boundary, ascending into a region of descending fluid, with a saddle-point at $(x/z_*=0,\ z/z_*=11/31)$.

The stochastic estimates depicted here are not perfectly symmetric owing to the fact that the mean was not subtracted from the velocities, and that symmetries were not forced during the calculation of the two-point correlations. Yet, the degree of symmetry of the stochastic estimates, which reflects the symmetric nature of the two-point correlations, is extremely high suggesting adequate convergence of these statistical quantities, and the absence of a discernible mean flow.

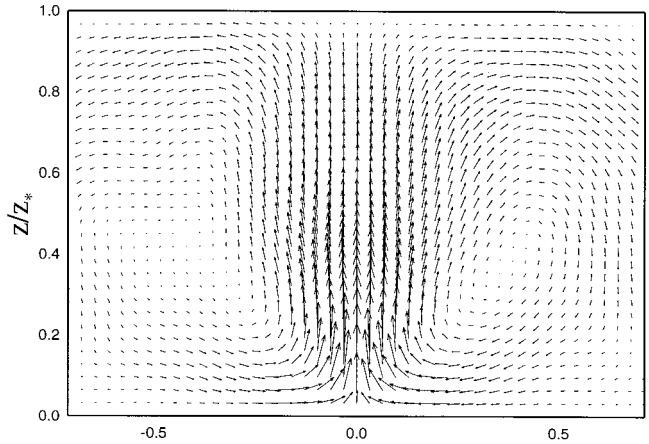

FIG. 11. Single point stochastic estimate with event vector (0,1) located at $(x/z_*=0,\ z/z_*=2/31)$.

IV. CONCLUSIONS

PIV measurements have been conducted for nonpenetrative convection in a water layer of aspect ratio of 6.6. A large data-set of two-dimensional velocities in a vertical plane has been obtained for $\mathrm{Ra}=2\times10^7$. The mean velocity profiles indicate the absence of a large-scale or global circulation, contrary to the observations of some previous researchers. Instead, underlying the seemingly chaotic flow is a roll-cell structure with unit aspect ratio, i.e., its horizontal dimension is equal to the depth of the fluid layer. This roll-cell structure is not obvious from flow visualization but emerges upon computing two-point correlations.

Stochastic estimates have been obtained based on the two-point correlation statistics. The estimated velocity field based on a single point event $(u,v)=(1,0)$ located at $z/z_*=2/31$ clearly reveals the unit aspect ratio roll cell. When a two-point event is specified $(u,v)=(0,1)$ located at $z/z_*=2/31$ and $(u,v)=(0,-1)$ located at $z/z_*=16/31$, the estimated velocity field indicates the presence of a plume forming along the lower boundary. The head of the plume is identified by a saddle point, and the horizontal velocities feeding the plume adjacent to the lower boundary are evident. Thus while the individual realizations present a rather disordered and chaotic flow, the statistical analysis indicates a unit-aspect ratio roll cell punctuated by thermal plumes.

If the specified event is a vertical vector $(u,v)=(0,1)$ located at $z/z_*=2/31$, then the stochastically estimated velocity field indicates a vertical plume which extends all the way to the upper boundary. Such an extended plume, stretching from the lower boundary all the way to the upper boundary is consistent with the measured vertical velocity skewness $S_w(z)$, which is always positive, and in fact increases with z near the upper boundary. The S_w profile is consistent with atmospheric measurements and large eddy simulations of the atmosphere.

[1] J. C. Wyngaard, ''Atmospheric turbulence,'' Annu. Rev. Fluid Mech. **24**, 205 (1992).
[2] J. W. Deardorff, G. E. Willis, and D. K. Lilly, ''Laboratory investigation of non-steady penetrative convection,'' J. Fluid Mech. **35**, 7 (1969).

[3]A. Cenedese and G. Querzoli, ''A laboratory model of turbulent convection in the atmospheric boundary layer,'' Atmos. Environment **28**, 1901 (1994).
[4]C.-H. Moeng and R. Rotunno, ''Vertical-velocity skewness in the buoyancy-driven boundary layer,'' J. Atmos. Sci. **47**, 1149 (1990).
[5]C.-H. Moeng and J. C. Wyngaard, ''Spectral analysis of large-eddy simulations of the convective boundary layer,'' J. Atmos. Sci. **45**, 3573 (1988).
[6]B. Castaing, G. Gunaratne, F. Heslot, L. Kadanoff, A. Libchaber, S. Thomae, X.-Z. Wu, S. Zaleski, and G. Zanetti, ''Scaling of hard thermal turbulence in Rayleigh–Bénard convection,'' J. Fluid Mech. **204**, 1 (1989).
[7]R. Krishnamurti and L. N. Howard, ''Large-scale flow generation in turbulent convection,'' Proc. Natl. Acad. Sci. USA **78**, 1981 (1981).
[8]A. E. Deane and L. Sirovich, ''A computational study of Rayleigh–Bénard convection. Part 1. Rayleigh number scaling,'' J. Fluid Mech. **222**, 231 (1991).
[9]H. Park and L. Sirovich, ''Turbulent thermal convection in a finite domain. Part II. Numerical results,'' Phys. Fluids A **2**, 1659 (1990).
[10]S. Balachandar, M. R. Maxey, and L. Sirovich, ''Numerical simulation of high Raleigh number convection,'' J. Sci. Comput. **4**, 219 (1989).
[11]R. M. Kerr, ''Rayleigh number scaling in numerical convection,'' J. Fluid Mech. **310**, 139 (1996).
[12]R. J. Adrian, R. T. D. S. Ferreira, and T. Boberg, ''Turbulent thermal convection in wide horizontal fluid layers,'' Exp. Fluids **4**, 121 (1986).
[13]A. K. Prasad and R. J. Adrian, ''Investigation of non-penetrative thermal convection using stereoscopic particle image velocimetry,'' in *Optical Diagnostics in Fluid and Thermal Flow*, edited by S. S. Cha and J. D. Trolinger, Proc. SPIE **2005**, 667 (1993).
[14]Z. Sorbjan, ''Similarity scales and universal profiles of statistical moments in the convective boundary layer,'' J. Appl. Meteorol. **29**, 762 (1990).
[15]E. D. Siggia, ''High Rayleigh number convection,'' Annu. Rev. Fluid Mech. **26**, 137 (1994).
[16]X. Wu and A. Libchaber, ''Scaling relations in thermal turbulence: The aspect ratio dependence,'' Phys. Rev. A **45**, 842 (1992).
[17]G. Zocchi, E. Moses, and A. Libchaber, ''Coherent structures in turbulent convection, an experimental study,'' Physica A **166**, 387 (1990).
[18]R. J. Adrian, ''Particle imaging techniques for fluid mechanics,'' Annu. Rev. Fluid Mech. **23**, 261 (1991).
[19]A. K. Prasad and R. J. Adrian, ''Stereoscopic particle image velocimetry applied to liquid flows,'' Exp. Fluids **15**, 49 (1993).
[20]J. C. Wyngaard and J. C. Weil, ''Transport asymmetry in skewed turbulence,'' Phys. Fluids A **3**, 155 (1991).
[21]R. J. Adrian, ''Stochastic estimation of conditional structure: A review,'' App. Sci. Res. **53**, 291 (1994).